Optics & Laser Technology 165 (2023) 109574

Contents lists available at ScienceDirect

Optics and Laser Technology

journal homepage: www.elsevier.com/locate/optlastec

Full length article

Application-inspired additive manufacturing of Raman optics

Tobias Grabe [a,b,c,*], Tobias Biermann [a,c], Alexander Wolf [a,c], Jassim Al-Nuwaider [a], Henrik Krauss [a], Jannes August [a], Weijia Yu [a], Jannis Ben Heinz [a], Maximilian Bayerl [a], Ke Xu [d], Qiang Wang [e], Junjun Wu [d,f], Bernhard Roth [c,g], Wei Ren [d], Roland Lachmayer [a,b,c]

[a] Leibniz University Hannover, Faculty of Mechanical Engineering, Institute of Product Development, An der Universitaet 1, Hannover, 30823, Lower Saxony, Germany
[b] GROTESK – Additive Manufacturing of Optical, Thermal and Structural Components, An der Universitaet 1, Hannover, 30823, Lower Saxony, Germany
[c] Cluster of Excellence PhoenixD (Photonics, Optics, and Engineering – Innovation Across Disciplines), Welfengarten 1A, Hannover, 30167, Lower Saxony, Germany
[d] Department of Mechanical and Automation Engineering, The Chinese University of Hong Kong, 209 William M.W. Mong Engineering Building, Hong Kong, New Territories, Hong Kong Special Administrative Region of China
[e] Changchun Institute of Optics, Fine Mechanics and Physics, Chinese Academy of Sciences, Changchun, 130033, China
[f] Key Laboratory of Low-grade Energy Utilization Technologies and Systems and School of Energy and Power Engineering, Chongqing University, No. 174, Shazheng Street, Shapingba District, Chongqing, 400044, China
[g] Leibniz University Hannover, Hannover Centre for Optical Technologies, Nienburger Strasse 17, Hannover, 30167, Lower Saxony, Germany

ARTICLE INFO

Keywords:
Optics manufacturing
Multi-Jet Modeling (MJM)
Additive Manufacturing (AM)
Design for Additive Manufacturing (DfAM)
Raman spectroscopy

ABSTRACT

While additive manufacturing (AM) enables the production of versatile optical components, the limited knowledge of manufacturing processes makes the development of accurate simulation tools and evaluation criteria challenging. In this work, we present a novel approach to address the specific challenges in the AM of optics by designing and fabricating freeform probe lenses for Raman Spectroscopy (RS) using the Multi-Jet Modeling (MJM) printing process. We successfully integrate the lenses into an RS system and demonstrate their performance in detecting melamine with a maximum signal-to-noise ratio of 164^{+16}_{-14}. We outline the capabilities and limitations of the AM process and adapt simulations to reveal the potential impact of manufacturing tolerances and diffraction effects on layered optical components. Based on our results, we highlight the potential to develop novel design standards for the AM of optics, providing a platform for further exploration and investigation.

1. Introduction

Additive Manufacturing (AM) has been established in optics alongside conventional processes over the recent years. Complex structures and freeform surfaces, including internal cavities, can be efficiently manufactured using additive processes, allowing complex systems to be simplified and additional functions to be integrated. Applications range from the manufacturing of mounts and housings [1–4] to optical elements [5–8]. To exploit the potential of AM for optical elements and systems, manufacturing equipment that exists only as a laboratory setup is often used. Often, the transferability of the results is limited and cannot be applied to other contexts without restrictions.

The literature also presents results for additively manufactured components for optical fibers [9], scanning devices [10], and laser systems [11], which were produced with commercially available AM systems. The AM of transmissive optical components has been demonstrated using a number of processes. Among the commercially available techniques, Multi-Jet Modeling (MJM), in particular, has been used to create macroscopic optical elements [12–14]. Although the potential use of these optics has been demonstrated through one-off experiments, major challenges remain. In practice, considerable manufacturing tolerances and unusual optical properties resulting from the layer-by-layer manufacturing process prevent their effective use. Inhomogeneities in the volumes and at the surfaces of optical elements cause scattering [15]. Initial approaches to quantify such imperfections can already be found in the literature. Reichel et al. characterized the effects caused by surface scattering using non-transparent MJM-manufactured parts [16]. Kuo et al. analyzed the surface roughness that can be achieved by polishing planar components manufactured with the same process [17]. However, the relations among the AM process, its parameters and the optical characteristics of the components have not been sufficiently described. Also, computational models and their

* Corresponding author at: Leibniz University Hannover, Faculty of Mechanical Engineering, Institute of Product Development, An der Universitaet 1, Hannover, 30823, Lower Saxony, Germany.
E-mail address: grabe@ipeg.uni-hannover.de (T. Grabe).

https://doi.org/10.1016/j.optlastec.2023.109574
Received 10 November 2022; Received in revised form 25 April 2023; Accepted 4 May 2023
Available online 16 May 2023

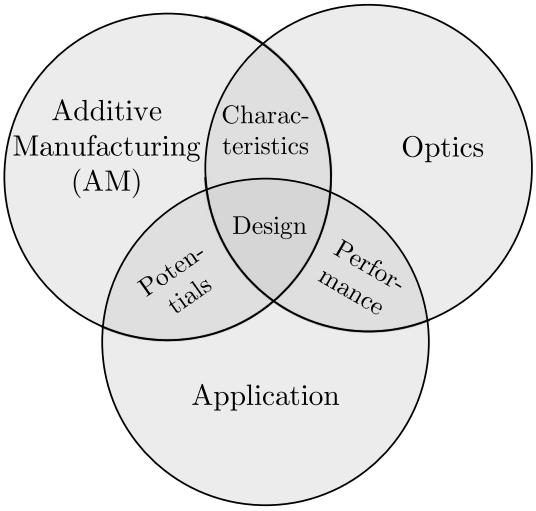

Fig. 1. The optics design as a key for combining AM and optics in an application context.

coupling with an optics design method are lacking so far. Consequently, the evaluation of the effects of the AM process on optical performance is usually limited to experimental analysis. Furthermore, tailored simulation approaches must be developed to create optics adapted explicitly to the specified AM process. Thus, in the context of this article, we demonstrate the analysis and synthesis steps, which are exemplarily shown in Fig. 1, using the collimation optics of a Raman spectrometer as an example.

Raman Spectroscopy (RS) can be applied in many fields, such as material sciences, pharmaceutical research, and biomedical applications [18]. One of the potential applications is in the pharmaceutical field for fast and onsite interrogation of SARS-CoV-2 via Surface-Enhanced Raman Scattering (SERS), as developed by Zhang and Ma by using an excitation laser with a wavelength of 785 nm [19]. In RS, photon energy variations caused by an inelastic scattering process are detected and evaluated.

Wavelengths of light ranging from ultraviolet to near-infrared can be used to excite Raman active molecules, from which a specific molecular vibrational information can be obtained [20]. Since the inelastically scattered signal is significantly smaller than the elastic one, sufficient scattered signal must be captured by the optical system for detection [21]. However, current approaches to increase the sensitivity of Raman systems focus on the interaction between excitation radiation and sample material. Concepts for increasing the collimation efficiency of the optical system can also enhance detection.

Using the possibilities of MJM as a manufacturing process for transmissive optics, we design freeform Raman lenses, which are capable of significantly increasing the collimation efficiency compared to a standard lens. We derive an optical concept methodology that takes the freeform manufacturing ability and the limitations of the AM process into account. Based on this methodology, we develop two different types of Raman probe lenses for a spectroscopic system. The properties of the additive manufactured optics are studied by detecting a selected model substance, i.e., melamine, and the impact factors on optical characteristics, which limit their applicability in optical systems, are discussed. Hereby, the particular potentials and challenges are worked out and are exemplary demonstrated based on the MJM process.

The paper is organized as follows. The fabrication setup, material properties and the lens design approach are introduced in Section 2. The Raman setup and the results for the lens performance are presented in Section 3. In Section 4, the impact of the manufacturing on the lens performance is derived in detail. The results are discussed in Section 5.

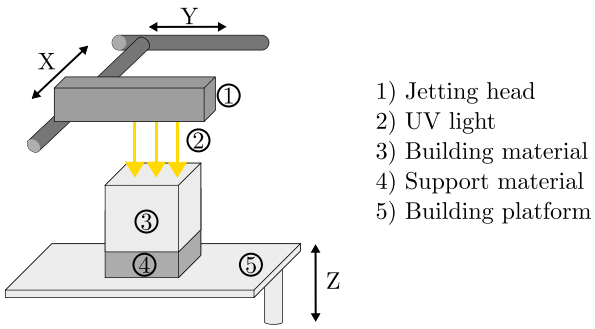

Fig. 2. Multi-Jet Modeling (MJM) process.

2. Methodology

2.1. Fabrication setup and materials

In this work, for the Raman probe lens manufacturing, an Objet30 Pro printer is used. The MJM process is shown in Fig. 2. The jetting head consists of 200 individual outlet nozzles, each with a diameter of 40 µm. They are arranged in a straight line along the Y-axis and the centers of the nozzles are 340 µm apart, covering a distance of 68 mm. In the printing process, the jetting head moves along the X-axis and is repositioned eight times along the Y-axis to complete a layer. Here, liquid photopolymer is dropped onto the printing platform and irradiated with an ultraviolet (UV) light source attached to the jetting head mechanism. The commercially available VeroClear RGD810 (Stratasys company) is used as the material. During printing, the jetting head is shifted along the Y-axis, and the droplet deposition process repeats. This procedure is carried out until a layer is entirely printed. With the accumulation of several photopolymer layers along the Z-axis, the object geometry is built up.

The resolution of the MJM process is anisotropic. In the horizontal plane, the resolution is 40 µm in the x- and y-direction, respectively. The specification of the vertical resolution in the z-direction is 16 µm. The transmittance of the material VeroClear RGD810 reaches its maximum for wavelengths of $\lambda = 715-1100$ nm [22]. Within this interval, the transmittance is more than 70% for a material thickness of 20 mm [17]. The refractive index of VeroClear RGD810 is given with $n = 1.531-1.518$ within the spectral range $\lambda = 632.8-1551$ nm [23].

Due to the layer-by-layer curing of the material, the optical properties of the component are affected. For transparent components, manufactured by MJM processes, anisotropic properties dependent on the printing direction are reported [10]. The transmittance for light with a wavelength of $\lambda = 420-650$ nm is comparatively low for propagation in the z-direction [17].

2.2. Optical design for Raman probe lenses

To precisely define the shape of each optically relevant freeform surface of the Raman lens, we use the so-called point-to-point redirection method [24] in a modified form [14]. This method is based on geometrical optics and creates profiles of reflective and refractive optical surfaces that are designed to guide light from a point source P_S to a point target P_T. A starting point $K_i, i = 0$ of the contour is required.

$$K_0 = \begin{pmatrix} K_{0,x} \\ K_{0,z} \end{pmatrix} \tag{1}$$

The subsequent point on the conical curve is then calculated with

$$K_{i+1} = \begin{pmatrix} K_{i,x} \\ K_{i,z} \end{pmatrix} + s \begin{pmatrix} t\cos(\alpha_t) \\ t\sin(\alpha_t) \end{pmatrix}, \tag{2}$$

where s is defined as −1 or 1 to set the direction of the surface construction. In this way, the functions of refraction and total internal reflection

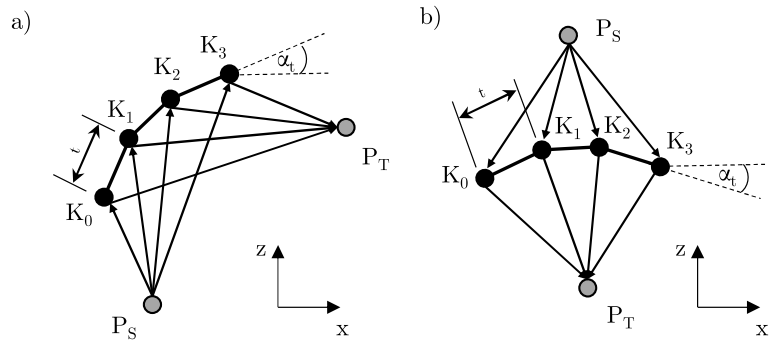

Fig. 3. Iterative construction of a reflective (a) and transmissive surface (b).

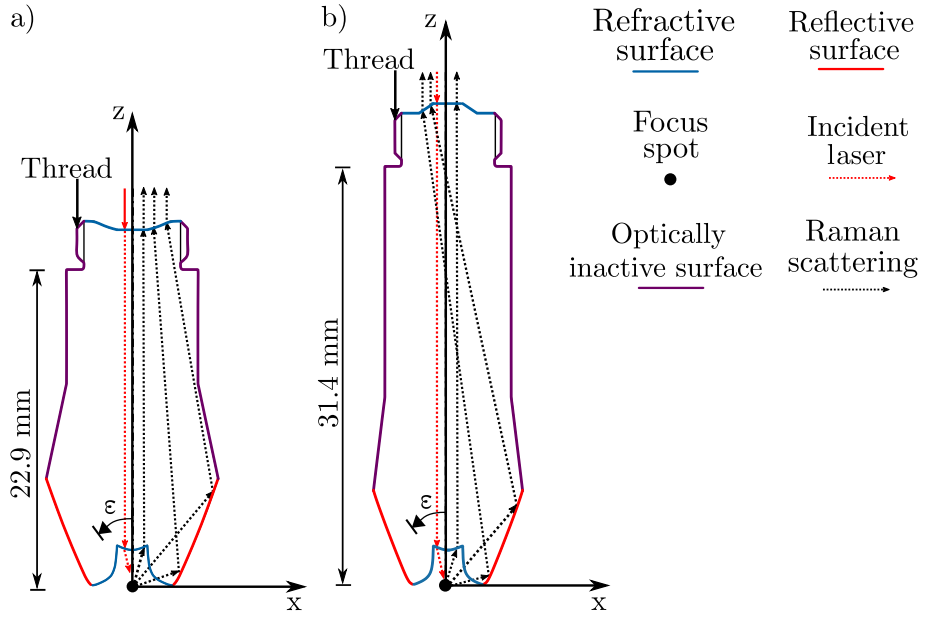

Fig. 4. Concept 1 (a) and 2 (b) of the additively manufactured lens. ϵ denotes the angle to the emitting surface normal.

can be assigned to different surface elements. t denotes the step size of the iteration, as well as the distance between two subsequent points. α_t denotes the tangential angle to the optical surface (see Fig. 3). In the design, manufacturing process-specific limitations, such as minimum radii of curvature r_{min} = 0.2 mm, are considered [25]. Since the optical system and its boundary conditions are rotationally symmetric, we design our lens in the x-z-plane and rotate it around the z-axis. Multiple surfaces are constructed sequentially to create the freeform shape for guiding the light through a non-imaging rotary symmetric optical element. The construction of these sequential optical surfaces is based on the definition of subsequent target points, where the first (virtual) target point is the starting point for the subsequential surface. Thus, several freeform surfaces can be combined to direct the light. Collimation of the light can be achieved by defining an infinitely distant target point.

Based on this principle, we propose two Raman lens concepts, which consist of a refractive center lens and an outer section using total internal reflection (see Fig. 4). The inner lens focuses the excitation laser on the sample and collimates the Raman scattering, while the outer section exclusively collimates the Raman scattering light with a wide acceptance angle. Both concepts are based on a refractive surface for the outer section and a collimation surface at the top. They include an optically inactive surface, on which an M8 x 0.5 thread is printed for mounting the lens on the Raman probe. The first concept (concept 1) uses a concave collimating surface, while the second concept (concept 2) reflects the scattering signal across the optical axis and uses a convex surface, which is easier to polish in a post-processing step. However, the propagation distance of the light beam through the medium is larger compared to concept 1.

The light collection efficiency of the Raman lens is considered, taking into account the Lambertian radiation characteristics of the excited sample and the Fresnel losses of the lens. In this work, several simplifications are initially made for a conceptual design, see below. The applicability of these assumptions is discussed in Section 4 based on the lens performance with regard to the special optical properties generated by the AM process. The following assumptions are made:

- Homogeneous and isotropic medium.
- Zero conductivity and magnetic permeability of the optical material, i.e., no absorption.
- Unpolarized light and no polarization changes within the lens.
- Ideal and smooth surfaces.

Since the raytracing is performed two-dimensionally for this rotationally symmetric optical element, a conversion of the results to three dimensions is required. The number of light rays in the 3-dimensional case increases with increasing angle ϵ relative to the emitting surface normal as $sin(\epsilon)$ [26]. Therefore, the Lambertian radiation pattern ($\propto cos(\epsilon)$) is weighted in the 2-dimensional model with a factor $sin(\epsilon) \cdot cos(\epsilon)$.

The light collection efficiency of the Raman lens (v_{eff}) is calculated by considering every interaction on each ray with the lens surface and its Fresnel losses. Partially reflected light rays are ignored. Rays

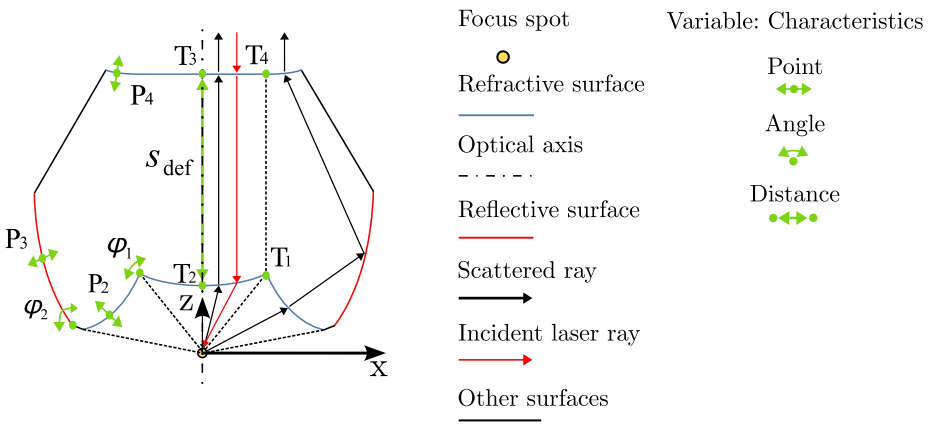

Fig. 5. Variable points and dimensions for optimization of the design concepts.

that miss the Raman lens are taken into account by reducing the lens efficiency. For optimization of the geometry, the parameters s_{def}, the angles φ_1, φ_2 and the points P_2, P_3 and P_4 can be modified, resulting in minor changes of the conic shapes. This principle is used to generate multiple variants of the lens geometry. The points T_1, T_2, T_3 and T_4 denote end points of optical surfaces, which are used in Section 4 for the impact analysis of manufacturing tolerances on the optical performance. The design points are shown in Fig. 5. Due to geometric restrictions, the distance between the radiation source and the first surface is set as 3 mm. To provide the optimum focus, the middle section is optimized for the laser wavelength $\lambda = 785$ nm. The outer one is based on total internal reflection and is optimized for $\lambda = 850$ nm, which corresponds to a Raman shift of $\Delta\nu = 974.15\,\mathrm{cm}^{-1}$, i.e., a scattered photon in the center of the expected Raman spectrum. The optically inactive surfaces can be designed as desired in the case of no interaction with the rays. In reality, the emission source of Raman scattering is not point-like. Therefore, a circular area with a radius of r_s ranging from −0.1 to 0.1 mm is described. The positioning tolerance along the optical axis is also considered, with a parameter of z_s ranging from −0.2 to 0.2 mm. The optimization goal is a Raman lens with a robust behavior with respect to deviations from the original assumptions. The average efficiency $\bar{v}_{\mathrm{eff}\ j}$ over this range of values is used to determine the optimization parameter q_j for each geometry variant j according to Eq. (3).

$$q_j = 1 - \bar{v}_{\mathrm{eff}\ j} \tag{3}$$

The optical elements perform better in guiding light onto the detector when q approaches zero. By repeatedly constructing the optical surfaces and applying a Nelder–Mead simplex algorithm to minimize q_j, the optics performance can be increased while minimizing the impact of the AM process tolerances. For concept 1, a maximum value of $v_{eff} = 0.8701$ is determined while for concept 2, the maximum value is $v_{eff} = 0.8488$ [14]. The resulting lens characteristics are shown in Fig. 6.

3. Manufactured Raman setup and performance

The reference RS system shown in Fig. 7 is built and used for the chemical analysis of melamine as an example substance to demonstrate its functionality. The general setup involves a FC-D 785 solid-state laser with a central wavelength of $\lambda_c = 785 \pm 0.5$ nm, a maximum optical output of $P_{\mathrm{Laser,max}} = 560$ mW and a spectral line width of 0.2 nm. The laser is connected to the RPB-785 Raman probe via an optical fiber with a core diameter of 100 µm. This probe has two integrated main functions. Firstly, it focuses the excitation laser on the test sample. Secondly, the Raman probe is required to collect the scattered light and guide the photons to a sensitive spectrometer (Maya 2000 Pro), which is connected to a computer for data acquisition.

The spectrometer covers the range 178 – 1100 nm, while the spectral range of the Raman probe is 796 – 1144 nm [14]. Since inelastically scattered photons are emitted with a longer wavelength than the excitation one, the spectral range between 796 and 1100 nm is of relevance here. As we implement the newly designed additively manufactured lens into an already existing system, some geometrical restrictions have to be considered. The excitation laser beam is initially collimated with a diameter of $d_L = 2$ mm and focused on the sample with a spot diameter of $d_f < 100$ µm. The collimation diameter of the Raman scattering signal is limited by the Raman probe construction to $d_s = 5$ mm. The Raman lens is required to be mounted on the Raman probe using an M8 thread. The material needs to be optically transparent for electromagnetic wavelengths between 785 λ 1100 nm. The actual Raman lens only allows a light collection angle of 37°. Thus, the freeform optics developed in this work are designed and implemented to increase this angle up to 160° by using the design method described in Section 2.2.

The probe lenses are manufactured by Multi-Jet-Modeling with an Objet30 Pro and VeroClear RGD810 material (Section 2.1). The following steps are involved in the manufacturing of the parts: First, the prototype designs are exported as an STL-file and placed on the building platform. Next, the lenses are orientated and sliced so that the layers are aligned orthogonal to the Z-axis (compare Fig. 4). Since the influence of the inactive optical surfaces on the performance of the component is expected to be negligible, the support material required for the manufacturing process is preferentially placed here. After the printing process, the optically functional surfaces are polished to optimize their performance [17]. No optical coating is applied on any part. For the evaluation of the prototypes, the measurement of a Raman spectrum is performed. Here, melamine (1,3,5-triazine-2,4,6-triamine) is chosen as the sample material. After the excitation at $\lambda = 785$ nm, melamine shows prominent peaks at 380, 580, 675, 775, 983, 1441 and 1554 cm^{-1} while the peaks at 675 cm^{-1} and 983 cm^{-1} are most pronounced and exhibit the highest Raman signal [27]. The peak at 675 cm^{-1} corresponds to the in-plane deformation of the triazine ring, while the peak at 984 cm^{-1} refers to the ring breathing mode 1 of the triazine ring [28]. In this work, the most prominent peak at 675 cm^{-1} is chosen for the quantitative analysis of the melamine spectra. To analyze the Raman signal, the strength of the peak is measured after the removal of the background and fluorescence signals [21,29]. For signal correction, the thermal shift of the spectrometer is compensated.

For each prototype concept, three identically constructed lenses are implemented into the spectrometer. The measurements are performed with an excitation laser power of $P_{\mathrm{Laser}} = 320.0 \pm 1.4$ mW and a signal integration time of $t_{\mathrm{int}} = 4{,}000$ ms. For each signal detection, $n_{\mathrm{sta}} = 50$ measurements averaged. The measurements of melamine are conducted by the implementation of both lens concepts into the Raman probe, which are placed 3 mm away from the scattering source. This results in a light gathering cone angle of more than 160°.

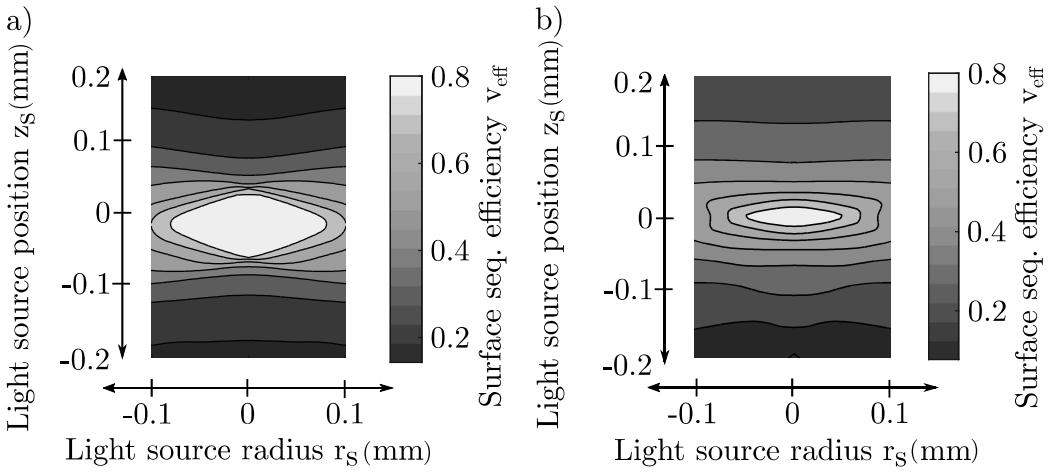

Fig. 6. Tolerance sensitivity results for concept 1 (a) and concept 2 (b) [14].

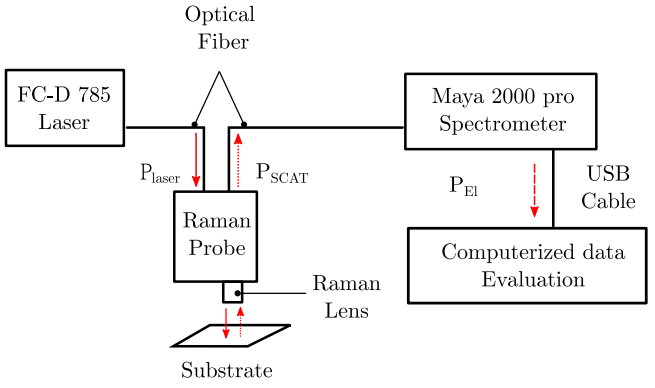

Fig. 7. Schematic structure of the Raman spectroscopy system. P_{Laser} denotes the optical laser power, P_{SCAT} the Raman scatter power and P_{El} the electric signal from the spectrometer.

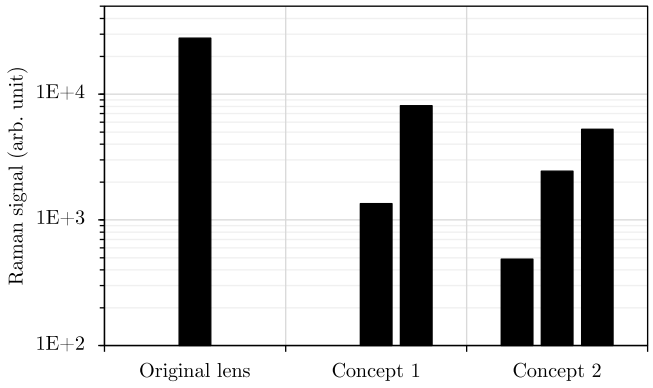

Fig. 8. Maximum Raman signals of the most significant 675 cm^{-1} peak of melamine achieved by the implementation of the manufactured prototype lenses from concept 1 and 2 in comparison with the original lens of the RPB-785 Raman probe.

The RS results for the additive manufactured lenses are shown in Fig. 8. In the experiment, Raman signal is measured for two lenses of concept 1 and for all three lenses of concept 2. For concepts 1 and 2 maximum Raman signals of $\bar{I}_{C1} = 8102$ and $\bar{I}_{C2} = 5255$ counts for the 675 cm^{-1} line of melamine are achieved. For the second lens of concept 1, the signal is 1350; for the second and third lenses of concept 2, the signals are 2438 and 488, respectively. In comparison, with the original glass lens of the Raman spectroscopy system a Raman signal of 27,983 counts can be detected. The Raman spectra are detailed in Supplement 1. The pixel-to-pixel noise is a characteristic of the spectrometer which is independent of the Raman lens itself and is determined with 49.4 ± 4.3 counts. This results in a maximum signal-to-noise ratio (SNR) for concept 1 and concept 2 of $SNR_{C1} = 164^{+16}_{-14}$ and $SNR_{C2} = 106^{+11}_{-9}$, respectively. Compared to the original lens of the RPB-785 Raman probe, concept 1 and concept 2 lenses achieved up to 29 % and 19 % of their performance, respectively. The Limit of Detection (LOD), which defines the minimal detectable Raman signal, is determined according to Eq. (4) [30].

$$LOD = 3 \cdot \sigma_{Noise} \tag{4}$$

A minimum signal of 148.2 ± 4.3 counts is required to consider a measured signal as significant. This criterion is fulfilled for each presented measurement.

4. Impact of the AM process on the lens performance

Considering the Raman signals shown in Fig. 8, the best melamine signal achieved with the lens from concept 1 is significantly stronger than the best result obtained with the lens from concept 2. Furthermore, in the implementation of the concept 2, a Raman signal is measured in three experiments, whereas for the concept 1, only two experiments were performed. From the experiment, it can be concluded that the quality of the additively manufactured optics is not fully reproducible and that a performance loss occurs compared to the original lens of the RPB-785 Raman probe. We attribute this to the influences of the MJM process on the quality of the optical elements. The imperfections of transmissive optical components can be divided into manufacturing tolerances, surface and volume imperfections, and the optical effects caused by the layer-by-layer manufacturing. Due to the AM process, the volume defects are sub-divided into inhomogeneities in the layers and inclusions, such as gas bubbles or dust. The superimposed influences of these errors can be seen, for example, in the asymmetrical widening of the laser spot behind the focal point, compare Fig. 9. Here, the scattered light of the incident laser is measured with a BC207VIS/M beam profiler at a distance of 11.4 mm after the focus point. The relative irradiance is determined linearly on the basis of the maximum irradiance measured on the sensor. In this measurement, unwanted scattering and diffraction effects can be observed.

4.1. Surface quality

The MJM processing of VeroClear RGD810 leads to visible periodic structures on the surfaces of the printed probe lenses. Using a Keyence VHX-900F confocal microscope, these surface structures can be measured, see Fig. 10. Since the surface structures and roughness result

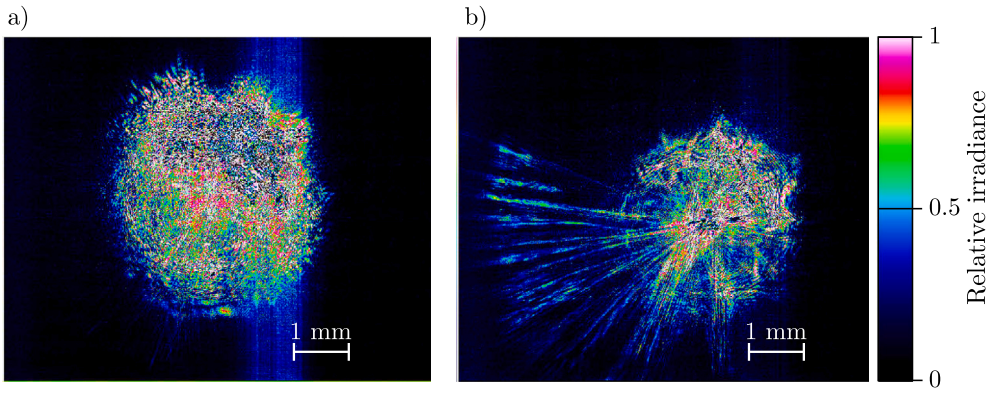

Fig. 9. Effects of optical scattering for the additively manufactured lens from concepts 1 (a) and 2 (b), respectively, when the beam cross sections are imaged at 11.4 mm after the designed collimation point.

Table 1
Surface roughness for plane surfaces dependent on their printing orientation manufactured by MJM.

	y-z-plane	x-z-plane	x-y-plane
Surface roughness Rq (µm)	1.56	0.41	8.77
Standard deviation σ_{Rq} (µm)	0.74	0.17	2.02

from the layer-wise building process, their properties are defined by the orientation on the building platform. Their scattering properties also depend on this orientation. According to ISO/ASTM 52902 [31], for measuring the roughness of planar surfaces, 15 samples with the dimensions $5 \times 8 \times 55\,mm^3$ are manufactured. Here, for each orientation, five samples are aligned along the X-, Y-, and Z-axes in the build space and distributed evenly over the platform. The surface of each sample is measured in five parallel lines using a tactile Mahr Perthometer PKG. The roughness is evaluated according to ISO 21920-3 [32] by separating and neglecting the periodic surface structure. The results are shown in Table 1. According to this data, the surface roughness R_q strongly depends on the building orientation and ranges between $0.41 - 8.77\,\mu m$. The Raman lens application wavelength is between 785 and 1100 nm. Thus, this roughness will lead to a significant optical scattering so that the functionality of the surfaces cannot be ensured without an additional reworking step. According to Harvey et al. [33] the fraction of the radiant power, that is scattered out of the specularly reflected beam due to the surface roughness, can be exemplarily described with the Total Integrated Scattering (TIS) model as

$$TIS = 1 - exp[-(4\pi \cdot cos\theta_i \cdot \sigma/\lambda)^2] \quad (5)$$

where θ_i is the incident angle, σ denotes the surface roughness (R_q) and λ is the wavelength of the incident beam [33]. A sigmoidal function describes the total scattering. The Raman spectrometer uses an excitation wavelength of 785 nm. Thus, for an incidence of light perpendicular to the optical surface, the TIS values approach the maximum limit at a roughness value of $R_q \leq 0.28\,\mu m$. In other words, for greater roughness, all the light incident on the lens surface is diffusely scattered, causing the lens to become dysfunctional. Based on this criterion, for functional optics, it is required to manufacture a surface roughness significantly smaller than $R_q = 0.28\,\mu m$. However, as shown in Table 1, this requirement is not achieved for any surface, regardless of how the optics are oriented on the building platform during the manufacturing process. It must also be considered that surfaces with support structures can only be finished with significant effort. Post-processing of the surfaces can be achieved, i.e., by chemical treatment, coating or spin-coating, honing, grinding as well as by robot-assisted or, as chosen in this work, manual polishing [34,35].

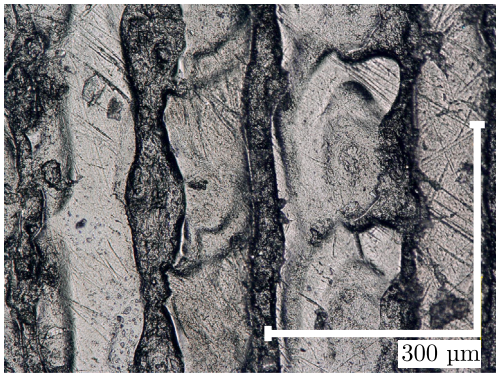

Fig. 10. Surface of the non-polished sample manufactured by MJM as observed by a Keyence VHX-900F confocal microscope.

4.2. Volume inclusions

Since the extruded resin is cured by UV light layer-by-layer, small inclusions from the manufacturing environment might attach to the optics and are then covered by the next layer. In addition, inclusions of gas bubbles can occur. Both defects lead to scattering and diffraction effects. Therefore, we also investigate the size distribution of these inclusions. A Keyence VHX-900F confocal microscope is used to detect and measure the size of 7515 inclusions in total. For the experiment, a planar polished test cube with the dimension of $25 \times 25 \times 25\,mm^3$ is analyzed by shifting the focal plane of the microscope. The inclusion diameters given in Fig. 11 is the maximum extent of an inclusion in the corresponding plane. The experiment is carried out in the middle of the volume to avoid surface effects. The resulting number of inclusion occurrences is normalized and categorized based on the size of the inclusions and the printing orientation of the sample. According to Fig. 11, the majority of the inclusions have an average diameter smaller than or equal to 2 µm. Since the resolution of the microscope is 1 µm, the actual number of these small inclusions is assumed to be even higher. The analysis shows that the distribution of the inclusions diameters differs depending on the printing direction of construction. Thus, the measured size of the inclusions is significantly smaller in the y-z-plane than in the other two planes. This leads to the conclusion that the shape of the inclusions is ellipsoidal. Furthermore, there is a predominant orientation of the inclusions, which depends on the orientation of the component during the building process. A more detailed analysis of these hypotheses is to be carried out in future work, as this affects the optical properties of the material. In general, inclusions of these sizes cause Mie or Rayleigh scattering [36]. Based on the inclusion size distribution shown in Fig. 11 and assuming the

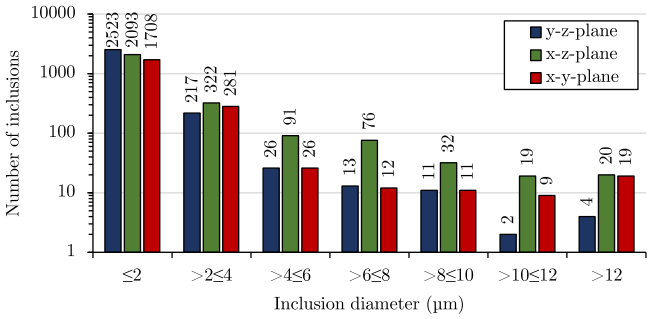

Fig. 11. Normalized occurrences of inclusions in the MJM-manufactured components as a function of the printing orientation based on a polished cubic reference specimen.

Table 2
Mean manufacturing deviation from the nominal dimension $\bar{m}$ and standard deviation from the mean value s for various structure sizes fabricated using the MJM process. The values for $\bar{m}$ and s are given in µm.

	Nominal dimension (mm)		
	2.5	12.5	55
$\bar{m}_x$ in x-direction (µm)	64.0	14.0	58.7
$\bar{m}_y$ in y-direction (µm)	15.0	−11.3	−19.7
$\bar{m}_z$ in z-direction (µm)	75.0	40.3	−148.0
s_x in x-direction (µm)	33.7	6.0	11.1
s_y in y-direction (µm)	14.2	4.5	2.2
s_z in z-direction (µm)	40.3	30.9	17.1

inclusion volume consists of air, this information is implemented in a Ray tracing simulation where Mie scattering is considered. According to Schmälzlin [37], the intensity of the Raman signal depends linearly on the irradiance of the excitation light on the sample. Thus, the area where the laser with an excitation laser power of $P_{\text{Laser}} = 320\,\text{mW}$ is focused on the melamine sample is analyzed regarding to the peak irradiance, the RMS spot radius and the total power on the sample surface in a $0.2 \times 0.2\ \text{mm}^2$ area. The results for concept 1 are shown in Fig. 12.

Up to a density of 10,000 inclusions per cubic centimeter, the peak irradiance is only slightly reduced and the effect on the RMS spot radius is negligible. From this result, it can be concluded that, the influence of volume inclusions on the performance of the optics is comparatively small but not negligible. Further, it is observed that single, larger inclusions in the light path can scatter a greater fraction of the laser light. The size, above which a volume defect is considered as critical for the optics functionality, has yet to be defined for AM. Thus, this aspect is of importance for the future AM of optics.

4.3. Manufacturing tolerances

In AM, the real component dimensions often deviate from the design values. This factor can affect the optics function. To quantify the deviation of the MJM process, which is used for lens manufacturing, the linear test body from ISO 52902 [31] is adapted. This benchmark geometry is displayed in Supplement 2. As suggested in ISO 52902, the parts are measured in less than 24 h after the AM process is finished. Five parts for each building direction (x, y, z) are manufactured within one print. For better accessibility during measurements, the produced parts are removed from the building platform. On each part three different feature sizes are measured to gain insight into statistical deviations and reproducibility. The results for the mean deviation $\bar{m}$ and its related standard deviation s for three different structure sizes and building directions are listed in Table 2.

The results show that the manufacturing tolerances are in the range of several micrometers. It can be interpreted that for a structural size of 12.5 mm a significantly lower deviation from the design can be achieved in comparison to smaller and larger geometries. In particular, the deviation in the z-direction is strongly affected by the size of the component. The lowest standard deviations are for each feature size observed in the y-direction, indicating that manufacturing results for this dimension may be more reproducible than in the x- and z-directions. The effects of these tolerances are elaborated with a simulation of the focal point of the lens of concept 1. For this purpose, the design points $T_1 - T_4$ (compared to Fig. 5) are shifted in x-, y- and z-direction according to the dedicated tolerances. The shifts are aimed to cover the 95 % tolerance interval. The manufacturing tolerances depend on the feature size and thus on the geometry of the lens in the respective printing direction. Both feature sizes between T_1 and T_2 as well as T_3 and T_4 is 2.3 mm. These sizes are smaller than the minimum nominal dimension of 2.5 mm defined in ISO 52902 for the test body. Therefore, for the x-y-deviation of these design points the feature size of 2.5 mm is considered. Thus, for the tolerance analysis in x-direction $x_{max} = \bar{m}_{x2.5} + 2 \cdot s_{x2.5}$ and in y-direction $y_{min} = \bar{m}_{y2.5} - 2 \cdot s_{y2.5}$ is simulated. In the z-direction, the distance between T_2 and T_3 is 23.2 mm, while T_1 and T_4 are 22.9 mm apart. For tolerance analysis in the z-direction, we consider values of $z_{min} = \bar{m}_{z23.2} - 2 \cdot s_{z23.2}$ for the points T_2 and T_3, and $z_{min} = \bar{m}_{z22.9} - 2 \cdot s_{z22.9}$ for T_1 and T_4. The values for $\bar{m}_{23.2}$ and $s_{23.2}$ and $\bar{m}_{22.9}$ and $s_{22.9}$ are linearly interpolated from Table 2. The irradiance distributions at the focal point on the detector, which is placed at the sample position, are shown in Fig. 13. For all deviations, the maximum tolerance results in a change in a power loss of less than 0.2%. From the simulation, it can be estimated that the tolerances in the z-direction have only a minor effect on the system performance for concept 1. Further, the r_{rms} spot diameter changes from 30.4 µm without deviation to 32.1 µm for z_{max} and 33.1 µm for z_{min}. Since the optics are printed along the z-direction to focus collimated light, only a small influence is expected here despite the comparably large manufacturing tolerance, which is reflected in this result. For the deviation in the x-direction, spot diameters of 160.0 µm for x_{max} and 30.9 µm for x_{min} and deviations in the y-direction of 63.9 µm for y_{max} and 36.4 µm for y_{min} are calculated. The results show a notable reduction in irradiance at the focus, particularly for larger spot diameters. This negatively affects the function of the optics and must to be considered for the future development of optics design concepts. Furthermore, Fig. 13 shows that the tolerances strongly affect the maximum irradiance on the sample. In particular, the manufacturing deviations in the x- and y-direction influence the result so that irradiance values of $7.87 \cdot 10^7\ \frac{W}{m^2}$ and $8.42 \cdot 10^8\ \frac{W}{m^2}$ can be achieved. These widely differing values mean that the tolerances can significantly influence the strength of the generated Raman signal.

4.4. Manufacturing layers

The optical properties of the material change with the layer-by-layer hardening. This characteristic is individual for each process and its settings. To analyze these effects, a polished test cube with the dimensions $25 \times 25 \times 25\,\text{mm}^3$ is irradiated with a laser from different directions. In this way, the light deflection caused by the layered structure and the volume inclusions become visible. A 0.72 mm wide Gaussian laser beam with a wavelength of 632 nm and an ellipticity of 95% is directed onto the cubic samples. The scattering profiles are captured on a plane at a distance of 143 mm from the light-emitting surface. The results are shown in Fig. 14. The scattering profile strongly depends on the layer orientation within the sample. This orientation is described in Section 2. A strong diffraction pattern is observed in the x- and y-directions, whereas little diffraction is visible in the z-direction.

An explanation for the diffraction effect is that the refractive index of the material depends on the progression of the polymerization [38]. Thus, a refractive index step can occur at the interface between layers. To estimate the impact of these volume effects on the optics presented in this work, the experimental setup for the MJM reference models

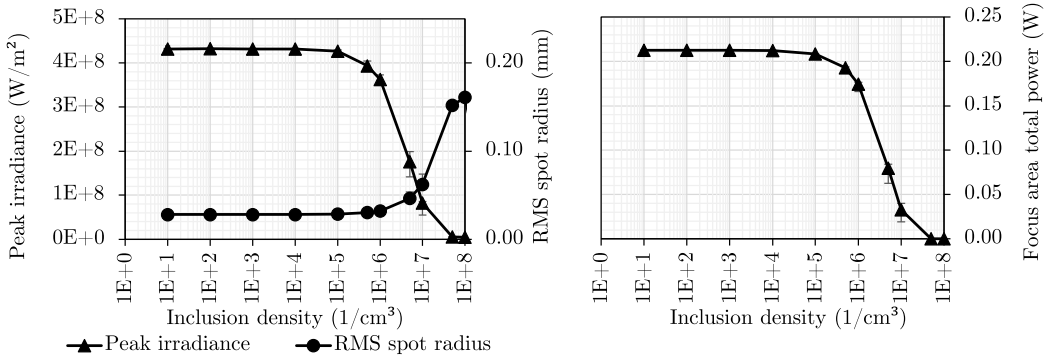

Fig. 12. Estimated impact of scattering caused by volume inclusions on the peak irradiance, RMS spot radius and laser power on the melamine sample for the lens of concept 1. The excitation laser power is $P_{\text{Laser}} = 320\,\text{mW}$.

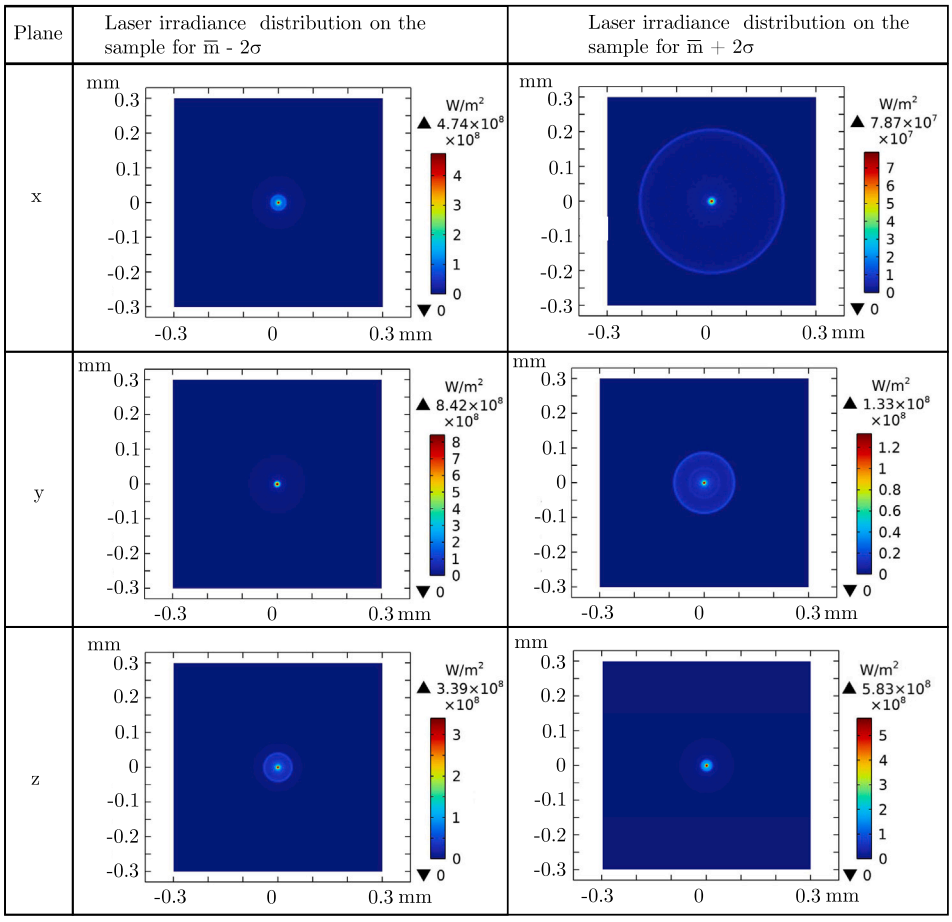

Fig. 13. Comparison of the simulated irradiance distributions for concept 1 at the focus point on the sample considering the maximum and minimum 2σ deviations regarding the points T_1 – T_4.

is replicated in a simulation, which is implemented in Comsol Multiphysics. The elements and parameters of this model are then applied to the into-the-lens simulation to estimate their impact in the optics performance.

In the simulation, the materials transmittance, refractive index, and distances to the projection surfaces are considered. The aim is to form a similar diffraction profile as a result of the volume structure of the cubic sample. This is achieved by applying gratings based on the specified grating constant, the diffraction order, and incident light wavelength. These gratings are aligned parallel to and positioned on the surfaces of the corresponding test cube. A grating is used to simulate the x- and *y*-direction diffraction with a lattice constant of 16 μm, which corresponds to the layer thickness of the cubic structure. A cross grating is used to simulate the *z*-direction plane where the lattice constant on both periodic directions is chosen to be 40 μm, which is the diameter of interconnected resin droplets used to form each layer. For both gratings the number of simulated diffraction orders is fitted to recreate the full width half maximum (FWHM) profile width of the cubic sample. Due to this fitting, the reference model can only represent the analyzed transmission length. The scattering profile widths can then be compared to the width of the intensity profile of the simulation, as shown in Table 3. A detailed comparison between the measurement and this simulation is shown in Supplement 3. These elements are applied to the lens to approximate the optical effects created by the

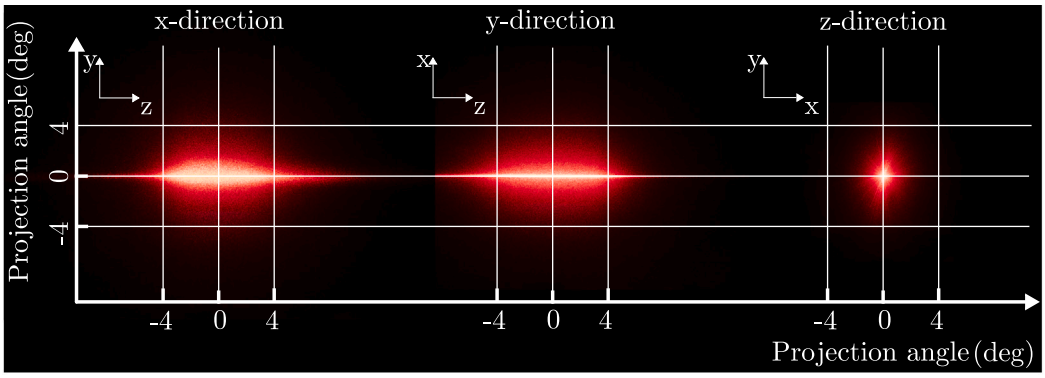

Fig. 14. Anisotropic optical scattering in additive manufactured component processed by Multi-Jet Modeling with a layer height of 16 µm.

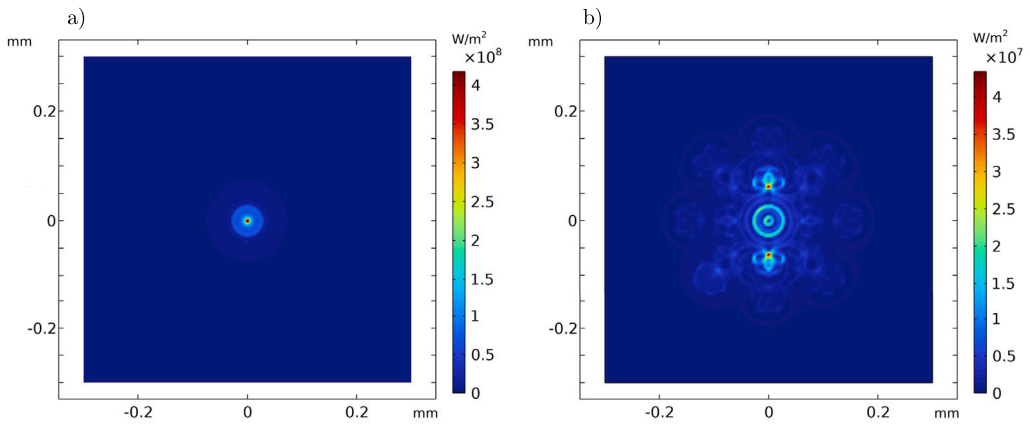

Fig. 15. Simulation of the laser focus spot for concept 1 (a) without anisotropic effects and scattering and (b) considering the anisotropic scattering in z-direction according to the diffraction theory.

Table 3
Comparison between the measured and the simulated scattering intensity profiles. The measured profile width is given as the full width at half maximum (FWHM) and the full width at tenth maximum (FWTM).

Illumination direction	Scatter profile direction	Measured FWTM/FWHM (mm)	Simulated FWTM/FWHM (mm)	Deviation (%)
x	y	11.0/9.2	10.6/9.2	3.6/0.0
	z	50.0/22.9	49.0/22.9	2.0/0.0
y	x	10.0/5.5	10.6/5.5	6.0/0.0
	z	60.0/34.1	60.0/34.1	0.0/0.0
z	x	12.0/3.7	10.6/3.7	11.7/0.0
	y	12.0/4.0	10.6/4.0	11.7/0.0

layer structure. It should be noted that the lens from concept 1 is analyzed here since the geometrical light path of the excitation laser through the lens is between 22.9 and 23.2 mm, which is considered to be similar to the 25 mm of the cubic sample. The simulation results for the laser focus spot on the sample for concept 1 printed along the z-direction with and without the implementation of anisotropic effects are shown in Fig. 15. Compared to the design case, the results show that diffraction increases the focus spot size and generates several local maxima. The presence of different layers causes diffraction, resulting in a maximum irradiance on the sample that is approximately 10 % of the one without such effects. Additionally, this factor causes in a reduction of approximately 37.5% of the total power on the evaluated surface.

5. Discussion

The detection of Raman signals demonstrates the potential of functional optics for rapid prototyping and use in Raman Spectroscopy (RS). However, we find that the layer-by-layer build nature and manufacturing imperfections of the Additive Manufacturing (AM) process significantly impact the characteristics and performance of the optics. Thus, the manufacturing quality and build-orientation-dependent optical effects are investigated to derive representative models for analyzing the AM-specific impact on the optics performance. The representative models presented in this study are discussed because they provide valuable insight into the limitations and potential for future development of additively manufactured bulk optics.

We analyze the surface roughness by considering different printing directions and fundamentally extending experimental considerations of Kuo et al. [17] and connecting the results to the TIS model to estimate its impact on the optics performance. While initial approaches for the analytical description of optical scattering occurring in Multi-Jet Modeling (MJM)-manufactured components are described by Rank et al. [12] and Horsak et al. [15], we further derive a simulation that explicitly describes these effects for multiple printing directions. Furthermore, the model accuracy is estimated quantitatively and implemented into a freeform optics simulation. Integrating the volume inclusions and manufacturing tolerances in a performance evaluation for additively manufactured lenses represents a novel approach.

The results of our study are subject to some uncertainties. For the analysis of the anisotropic effects, a sample with a geometrical propagation path of 25 mm is evaluated. However, the geometrical propagation path and wavelength propagating through the lenses may deviate from this experimental setup and fractionally impact the performance analysis results. For the consideration related to the surface roughness, the periodic structures on the surface generated by the MJM process are neglected. However, these structures may act as microlenses and cause additional optical scattering. Furthermore, the effects of post-processing and the aging behavior of the optics were not considered. These factors will influence the performance because, in particular, the spectral transmittance may change [17]. The significant benefit of our study is that all reported analyses, simulations, and experiments are limited to a single manufacturing process and material, excluding uncertainties in the data caused by using different machines, suppliers, and post-processing methods. Further, the applicability and performance of the AM optics are quantitatively validated to support the presented approach and results.

The impact of each specific factor resulting from the AM process on the lens performance varies significantly. As a result, the surface quality generated by the MJM process needs to be improved for the presented applications. Hence, post-processing is required. The selection of suitable finishing processes and their systematic integration into the AM process chain in the form of sequential or hybrid processes are important [35,39] but have yet to be established. In our study, the anisotropic optical effects reduce the maximum irradiance on the sample to about 10 % of the value for isotropic material. This result indicates that with a design methodology that considers the anisotropic effects, a significant increase in the maximum performance of the optics may be achieved. However, in order to minimize these losses, the design of the optics must be adapted. Therefore, in future work, more detailed models for simulating the material and improved design approaches for optimizing the geometry have to be developed. Further, we show that the manufacturing tolerances potentially lower the maximum irradiance achieved on the sample to 18 % of the designed value. These results demonstrate that developing practical guidelines for the optimal orientation, and carrying out targeted tolerance analysis is recommended to ensure the optimum functionality in additive manufactured optics. They further indicate that a tailored lens design that mitigates the negative impact of the tolerances may improve the experimental repeatability of the results [40]. The success of our approach indicates the potential to use photopolymerization-based processes for rapid prototyping of freeform lenses that can be integrated into an RS system. This opens up opportunities to develop advanced optics for various applications, including production monitoring [41], environmental analytics, and life sciences [42,43].

6. Conclusion

Despite the promising potential of Additive Manufacturing (AM) in optics demonstrated in this study, achieving high precision and desirable optical properties remains a significant challenge. This topic represents a promising field for further research. Our study investigated manufacturing quality and orientation-dependent optical effects to derive representative models for analyzing AM-specific influences on optics performance. The results suggest that considering anisotropic optical properties and tolerance analysis in the design environment can improve optical designs for optimal functionality. For the presented application in Raman Spectroscopy (RS), improving the surface quality generated by the AM process requires a comprehensive approach that includes both advances in the AM process and the development of tailored post-processing techniques. These findings have significant implications for the future development of additively manufactured bulk optics for various applications. Therefore, further research should focus on the development of tailored simulation approaches for the design and optimization of optical components adapted to the specific AM processes and application scenarios in order to fully exploit the potential of the AM for optics.

CRediT authorship contribution statement

Tobias Grabe: Conceptualization, Data curation, Formal analysis, Investigation, Methodology, Validation, Writing – original draft, Writing – review & editing. **Tobias Biermann:** Methodology, Writing – review & editing. **Alexander Wolf:** Methodology, Writing – review & editing. **Jassim Al-Nuwaider:** Formal analysis. **Henrik Krauss:** Formal analysis. **Jannes August:** Formal analysis. **Weijia Yu:** Formal analysis. **Jannis Ben Heinz:** Formal analysis. **Maximilian Bayerl:** Formal analysis. **Ke Xu:** Supervision, Writing – review & editing. **Qiang Wang:** Supervision, Writing – review & editing. **Junjun Wu:** Supervision, Writing – review & editing. **Bernhard Roth:** Writing – review & editing. **Wei Ren:** Conceptualization, Funding acquisition, Investigation, Methodology, Project administration, Supervision, Writing – original draft, Writing – review & editing. **Roland Lachmayer:** Conceptualization, Funding acquisition, Investigation, Methodology, Project administration, Supervision, Writing – review & editing.

Declaration of competing interest

The authors declare that they have no known competing financial interests or personal relationships that could have appeared to influence the work reported in this paper.

Data availability

Data will be made available on request.

Acknowledgments

Parts of this work were done within the projects “GROTESK - Generative Fertigung optischer, thermaler und struktureller Komponenten”, funded by EFRE - NBank [ZW6-85018307], and the Cluster of Excellence PhoenixD [EXC 2122, Project ID 390833453] funded by the Deutsche Forschungsgemeinschaft (DFG, German Research Foundation) within Germany’s Excellence Strategy.

Appendix A. Supplementary data

Further details on specific aspects of this paper can be found in the supplementary material: Supplementary material 1 for information about the detected Raman spectra. Supplementary material 2 for geometrical information of the tolerance benchmark geometry. Supplementary material 3 for information about comparing the measurement and the simulation of the anisotropic optical properties.

Supplementary material related to this article can be found online at https://doi.org/10.1016/j.optlastec.2023.109574.

References

[1] D.P.G. Nilsson, T. Dahlberg, M. Andersson, Step-by-step guide to 3D print motorized rotation mounts for optical applications, Appl. Optics 60 (13) (2021) 3764–3771, http://dx.doi.org/10.1364/AO.422695.

[2] M. Delmans, J. Haseloff, μ Cube: A framework for 3D printable optomechanics, J. Open Hardw. 2 (1) (2018) 1–9, http://dx.doi.org/10.5334/joh.8.

[3] L.J. Salazar-Serrano, J. P. Torres, A. Valencia, A 3D printed toolbox for opto-mechanical components, PLoS One 12 (1) (2017) e0169832, http://dx.doi.org/10.1371/journal.pone.0169832.

[4] J. Röttger, T. Grabe, M.C. Sundermeier, F. Kranert, O. Heizmann, T. Biermann, A. Ziebehl, P.-P. Ley, A. Wolf, R. Lachmayer, Additive manufacturing of a laser heat sink: Multiphysical simulation for thermal material requirement derivation, in: R. Lachmayer, B. Bode, S. Kaierle (Eds.), Innovative Product Development By Additive Manufacturing 2021, Springer International Publishing, Cham, 2023, pp. 183–198, http://dx.doi.org/10.1007/978-3-031-05918-6_12.

[5] W. Kang, Z. Hong, R. Liang, 3D printing optics with hybrid material, Appl. Optics 60 (7) (2021) 1809–1813, http://dx.doi.org/10.1364/AO.414406.

[6] K. Weber, D. Werdehausen, P. König, S. Thiele, M. Schmid, M. Decker, P.W. de Oliveira, A. Herkommer, H. Giessen, Tailored nanocomposites for 3D printed micro-optics, Opt. Mater. Exp. 10 (10) (2020) 2345, http://dx.doi.org/10.1364/OME.399392.

[7] K. Weber, Z. Wang, S. Thiele, A. Herkommer, H. Giessen, Distortion-free multi-element hypergon wide-angle micro-objective obtained by femtosecond 3D printing, Optics Lett. 45 (10) (2020) 2784–2787, http://dx.doi.org/10.1364/OL.392253.

[8] B.G. Assefa, T. Saastamoinen, M. Pekkarinen, V. Nissinen, J. Biskop, M. Kuittinen, J. Turunen, J. Saarinen, Realizing freeform lenses using an optics 3D-printer for industrial based tailored irradiance distribution, OSA Continuum 2 (3) (2019) 690, http://dx.doi.org/10.1364/OSAC.2.000690.

[9] A. Heinrich, P. Maillard, A. Suckow, A. Grzesiak, P. Sorg, U. Berger, Additive manufacturing: A new approach for individualized optical shape metrology, in: P. Lehmann, W. Osten, A. Albertazzi Gonçalves (Eds.), Optical Measurement Systems for Industrial Inspection IX, in: SPIE Proceedings, SPIE, 2015, p. 95251T, http://dx.doi.org/10.1117/12.2183168.

[10] A. Heinrich, M. Rank, 3D printing of optics, in: A. Heinrich, M. Rank (Eds.), 3D Printing of Optics, SPIE, 2018, http://dx.doi.org/10.1117/3.2324763.ch1.

[11] F. Kranert, J. Budde, P. Neef, R. Bernhard, M. Lammers, K. Rettschlag, T. Grabe, A. Wienke, J. Neumann, H. Wiche, V. Wesling, H. Ahlers, R. Lachmayer, D. Kracht, 3D-printed, low-cost, lightweight optomechanics for a compact, low-power solid-state amplifier system, in: A.L. Glebov, P.O. Leisher (Eds.), Components and Packaging for Laser Systems VI, SPIE, 2020, http://dx.doi.org/10.1117/12.2544268.

[12] M. Rank, A. Sigel, Y. Bauckhage, S. Suresh-Nair, M. Dohmen, C. Eder, C. Berge, A. Heinrich, 3D printing of optics based on conventional printing technologies, in: A. Heinrich (Ed.), 3D Printing of Optical Components, in: Springer Series in Optical Sciences, vol. 233, Springer International Publishing, Cham, 2021, pp. 45–167, http://dx.doi.org/10.1007/978-3-030-58960-8_3.

[13] H.Y. Jeong, E. Lee, S.-C. An, Y. Lim, Y.C. Jun, 3D and 4D printing for optics and metaphotonics, Nanophotonics 9 (5) (2020) 1139–1160, http://dx.doi.org/10.1515/nanoph-2019-0483.

[14] T. Grabe, Y. Li, H. Krauss, A.G. Wolf, J. Wu, C. Yao, Q. Wang, R. Lachmayer, W. Ren, Freeform optics design for Raman spectroscopy, in: Y. Soskind, L.E. Busse (Eds.), Photonic Instrumentation Engineering VII, SPIE, 2020, p. 10, http://dx.doi.org/10.1117/12.2544708.

[15] A. Horsak, A. Heinrich, M. Rank, Simple scattering analysis and simulation of optical components created by additive manufacturing, in: J.L. Bentley, S. Stoebenau (Eds.), Optifab 2017, SPIE, 2017, http://dx.doi.org/10.1117/12.2279781.

[16] S. Reichel, K. Blankenbach, F. Spaeth, V. Wohlgemuth, A. Reber, M. Rank, A. Heinrich, Improved light scattering characterization by BSDF of automotive interior and 3D printed materials, in: Y. Soskind, L.E. Busse (Eds.), Photonic Instrumentation Engineering VIII, SPIE, 2021, http://dx.doi.org/10.1117/12.2578150.

[17] H.-J. Kuo, C.-Y. Huang, W.-H. Wang, P.-H. Lin, H.-L. Tsay, W.-Y. Hsu, The study on surface characteristics of high transmission components by 3D printing technique, in: A.K. Asundi (Ed.), Fifth International Conference on Optical and Photonics Engineering, in: SPIE Proceedings, SPIE, 2017, p. 104492B, http://dx.doi.org/10.1117/12.2270850.

[18] M. Jermyn, J. Desroches, K. Aubertin, K. St-Arnaud, W.-J. Madore, E. de Montigny, M.-C. Guiot, D. Trudel, B.C. Wilson, K. Petrecca, F. Leblond, A review of Raman spectroscopy advances with an emphasis on clinical translation challenges in oncology, Phys. Med. Biol. 61 (23) (2016) R370–R400, http://dx.doi.org/10.1088/0031-9155/61/23/R370.

[19] D. Zhang, X. Zhang, R. Ma, S. Deng, X. Wang, X. Wang, X. Zhang, X. Huang, Y. Liu, G. Li, J. Qu, Y. Zhu, J. Li, Ultra-fast and onsite interrogation of severe acute respiratory syndrome coronavirus 2 (SARS-CoV-2) in waters via surface enhanced Raman scattering (SERS), Water Res. 200 (2021) 117243, http://dx.doi.org/10.1016/j.watres.2021.117243.

[20] E. Smith, Modern Raman Spectroscopy: A Practical Approach, J. Wiley, ebrary, Inc, Hoboken, NJ, 2005, http://dx.doi.org/10.1002/0470011831.

[21] M. Schlösser, Accurate Calibration of Raman Systems, Springer Cham Heidelberg New York Dordrecht London, Karlsruhe Institute of Technology, Germany, 2014.

[22] C.-Y. Huang, C.-M. Chang, C.-F. Ho, T.-W. Lee, P.-H. Lin, W.-Y. Hsu, The research on surface characteristics of optical lens by 3D printing technique and precise diamond turning technique, in: A.K. Asundi (Ed.), Fifth International Conference on Optical and Photonics Engineering, in: SPIE Proceedings, SPIE, 2017, http://dx.doi.org/10.1117/12.2270466.

[23] V. Prajzler, P. Kulha, M. Knietel, H. Enser, Large core plastic planar optical splitter fabricated by 3D printing technology, Opt. Commun. 400 (2017) 38–42, http://dx.doi.org/10.1016/j.optcom.2017.04.070.

[24] J.-J. Chen, T.-Y. Wang, K.-L. Huang, T.-S. Liu, M.-D. Tsai, C.-T. Lin, Freeform lens design for LED collimating illumination, Optics Express 20 (10) (2012) 10984–10995, http://dx.doi.org/10.1364/OE.20.010984.

[25] C.W. Nicholas Meisel, An investigation of key design for additive manufacturing constraints in multimaterial three-dimensional printing, J. Mech. Design (137) (2015) http://dx.doi.org/10.1115/1.4030991.

[26] M. Born, E. Wolf, Principles of Optics: Electromagnetic Theory of Propagation, Interference and Diffraction of Light, sixth ed., reprinted (with corrections), Pergamon Press, Oxford, 1993.

[27] A.R.M. Radzol, K.Y. Lee, N.E. Abdul Wahab, Low concentration melamine detection with surface enhanced Raman spectroscopy, in: IEEE Region 10 Symposium, 2014, IEEE, Piscataway, NJ, 2014, pp. 555–559, http://dx.doi.org/10.1109/TENCONSpring.2014.6863096.

[28] E. Koglin, Adsorption and displacement of melamine at the Ag/electrolyte interface probed by surface-enhanced Raman microprobe spectroscopy, J. Phys. Chem. 100 (1996) 5078–5089.

[29] A. Jirasek, G. Schulze, M.M.L. Yu, M. Blades, R. Turner, Accuracy and precision of manual baseline determination, Appl. Spectrosc. 58 (12) (2004) 1488–1499.

[30] G. Long, J. Winefordner, Limit of detection. A closer look at the IUPAC definition, Anal. Chem. 55 (7) (1983) http://dx.doi.org/10.1021/ac00258a724.

[31] International Organization for Standardization, ISO/ASTM 52902:2019: Additive manufacturing — Test artifacts — geometric capability assessment of additive manufacturing systems, 2022, 25.030 Additive Manufacturing.

[32] International Organization for Standardization, ISO 21920-3:2021: Geometrical product specifications (GPS) — Surface texture: Profile — Part 3: Specification operators, 2022, 17.040.40 Geometrical Product Specification (GPS).

[33] J.E. Harvey, Total integrated scatter from surfaces with arbitrary roughness, correlation widths, and incident angles, Opt. Eng. 51 (1) (2012) 013402, http://dx.doi.org/10.1117/1.OE.51.1.013402.

[34] A. Heinrich, M. Rank, P. Maillard, A. Suckow, Y. Bauckhage, P. Rößler, J. Lang, F. Shariff, S. Pekrul, Additive manufacturing of optical components, Adv. Opt. Technol. 5 (4) (2016) http://dx.doi.org/10.1515/aot-2016-0021.

[35] G. Leuteritz, R. Lachmayer, Additive manufacturing of reflective optics: evaluating finishing methods, in: H. Helvajian, B. Gu, A. Piqué (Eds.), Laser 3D Manufacturing V, in: Proceedings of SPIE, SPIE, Bellingham, Washington, USA, 2018, p. 24, http://dx.doi.org/10.1117/12.2289998.

[36] S. Asano, G. Yamamoto, Light scattering by a spheroidal particle, Appl. Optics 14 (1) (1975) 29–49, http://dx.doi.org/10.1364/AO.14.000029.

[37] E. Schmälzlin, B. Moralejo, M. Rutowska, A. Monreal-Ibero, C. Sandin, N. Tarcea, J. Popp, M.M. Roth, Raman imaging with a fiber-coupled multichannel spectrograph, Sensors (Basel, Switzerland) 14 (11) (2014) 21968–21980, http://dx.doi.org/10.3390/s141121968.

[38] M. Rank, A. Heinrich, Measurement and use of the refractive index distribution in optical elements created by additive manufacturing, in: G. von Freymann, W.V. Schoenfeld, R.C. Rumpf (Eds.), Advanced Fabrication Technologies for Micro/Nano Optics and Photonics XII, in: Proceedings of SPIE, SPIE, Bellingham, Washington, USA, 2019, p. 35, http://dx.doi.org/10.1117/12.2507262.

[39] Z. Zhu, V.G. Dhokia, A. Nassehi, S.T. Newman, A review of hybrid manufacturing processes – state of the art and future perspectives, Int. J. Comput. Integr. Manuf. 26 (7) (2013) 596–615, http://dx.doi.org/10.1080/0951192X.2012.749530.

[40] J. DeGroote Nelson, R.N. Youngworth, D.M. Aikens, The cost of tolerancing, in: J. Sasián, R.N. Youngworth (Eds.), Optical System Alignment, Tolerancing, and Verification III, in: SPIE Proceedings, SPIE, 2009, p. 74330E, http://dx.doi.org/10.1117/12.828433.

[41] A. Farooq, A.B. Alquaity, M. Raza, E.F. Nasir, S. Yao, W. Ren, Laser sensors for energy systems and process industries: Perspectives and directions, Prog. Energy Combust. Sci. 91 (2022) 100997, http://dx.doi.org/10.1016/j.pecs.2022.100997.

[42] A.-K. Kniggendorf, C. Wetzel, B. Roth, Microplastics detection in streaming tap water with Raman spectroscopy, Sensors (Basel, Switzerland) 19 (8) (2019) http://dx.doi.org/10.3390/s19081839.

[43] M. Mazurenka, L. Behrendt, M. Meinhardt-Wollweber, U. Morgner, B. Roth, Development of a combined OCT-Raman probe for the prospective in Vivo clinical melanoma skin cancer screening, Rev. Sci. Instrum. 88 (10) (2017) 105103, http://dx.doi.org/10.1063/1.5004999.